Published in final edited form as:
Nanoscale. 2012 July 21; 4(14): 4228–4233. doi:10.1039/c2nr30212h.

Grain Size Effects in Polycrystalline Gold Nanoparticles

Chen Zhou, **Jing Yu**, **Yanping Qin**, and **Jie Zheng***

Abstract

We report a structure-property relationship in gold nanoparticles (**NPs**), grain-size effects, which not only allow material properties observed on different characteristic length scales to be engineered in a single NP but further enhance those properties due to the coupling among different-size grains. The grain size effects were achieved by creating polycrystalline gold NPs (**pAuNPs**) with two distinct grain-size populations (5 and 1 nm) comparable to electron mean free path and electron Fermi wavelength (**EFW**) respectively. Successful integration of molecular and plasmonic properties into a single nanostructure without additional fluorophores enables these highly polycrystalline AuNPs to serve as multimodal probes in a variety of optical microscopic imaging techniques.

Introduction

Grain size effects have been widely observed from polycrystalline metallic thin films composed of grains with different sizes and orientations.[1–4] The decrease of grain size not only increases grain boundary scattering, but also results in emergence of quantum confinement effects (emergence of discrete energy states).[5–8] Consequently, grain size has been a critical structural parameter in tailoring material properties of metallic thin films. For example, due to grain-boundary scattering effects, a decrease in grain size often improves yield strength and hardness of materials[9–11] but reduces their electrical and thermal conductivities.[12–13] While single-crystal gold films generally have very small enhancements on the Raman scattering of organic molecules on their surfaces, the increase of surface roughness by decreasing grain size can dramatically enhance Raman-scattering cross sections of organic molecules on the gold surface[14]. Not only Raman scattering, other linear or nonlinear optical properties of metallic films, such as absorption, fluorescence as well as two-photon emission, also change accordingly with crystallinity and grain size.[15] In addition, grain boundaries together with surface defects also have significant influence on the catalytic properties of polycrystalline materials. For example, Tsybulya et al found that catalytic activity of supported silver catalysts in the ethylene epoxidation reaction increased substantially with the proportion of the gain boundary regions.[16]

In addition to grain boundary scattering, grain size effects also influence material properties of metallic thin films through quantum size effects. For example, it was found that when grain size of superconducting films became comparable to EFW, the transition temperature of the superconductor increased. This observation was attributed to the emergence of a discrete spectrum of one-electron energy levels once the grains size is decreased to EFW.[17]

Department of Chemistry, University of Texas at Dallas, 800 W Campbell Rd, Richardson, TX, 75080, USA. jiezheng@utdallas.edu; Tel: +1-972-883-5768; Fax: +1-972-883-2925.

†Electronic Supplementary Information (ESI) available: Supplementary figures of DLS, SAED, dark field image, fluorescence image, Raman image, SERS spectra and controll cell experiments etc. are included in the supporting information. See DOI: 10.1039/b000000x/

More recently, quantum confinement effects arising from decrease of grain size have also been observed in many other metallic thin film systems with tiny grain sizes.[12, 17–23]

Material properties of metal NPs can be judiciously tailored by tuning physical size of the particles. While very small metal NPs (20~50 nm) also exhibit polycrystalline structure, well-known particle-size effects often shadow grain size effects on material properties of metal NPs. Based on particle size, nanoscale metals are roughly classified into large NPs, small NPs, and clusters during atom-to-bulk transition, corresponding to three different characteristic length scales. Optical responses of large metal NPs ($R>\lambda$) to external electromagnetic fields can be quantitatively described with Mie theory.[24] When particle size approaches the electron mean free path (~50 nm for gold and silver), surface plasmons, Raman enhancements and other collective properties become strongly size-dependent. For example, decrease of particle size also results in the blue shift of surface plasmons, which can still be described with a modified Mie theory.[24–25] Eventually, when particle size becomes comparable to the third characteristic length - the Fermi wavelength of an electron (i.e. de Broglie's wavelength of an electron at the Fermi energy, or ~0.5 nm for gold and silver),[26–29] optical, electronic, and chemical properties of metal nanoclusters are dramatically different from the other two size regimes. In this smallest size regime, metal nanoclusters become "molecular species",[30–32] and discrete states with single electron excitations and strong fluorescence were observed,[33–36] following a well-known free electron model while surface plasmons and strong Raman enhancements start fading away.

While size effects in the metal NPs have been well understood in the past decades, only grain boundary scattering effect was recognized as an important factor for tuning optical properties and functionalities of already small silver NPs.[37] For example, grain boundary was found to greatly enhance electron-phonon interactions and dampen local surface plasmon resonance and decrease elastic modulus of the silver NPs.[37] However, how grain size influences material properties of metal NPs still have not been fully understood. A major roadblock for achieving a comprehensive understanding of grain-size effects in noble metal NPs is the lack of chemistry for precise control of grain size down to EFW.[24] To address this challenge, we recently developed a solid-phase thermal reduction method, which allowed us to create polycrystalline plasmonic silver NPs with grain size down to the EFW level.[38] These highly polycrystalline silver NPs exhibited bright, robust fluorescence that can be readily observed at the single particle level while the same size silver NPs with average grain size of ~8 nm are nonluminescent[38]. While these results indicate that optical properties of silver NPs are influenced by particle crystallinity, whether grain size effect is a general phenomenon in metal NPs is largely unknown. In addition, the applications of this new class of polycrystalline metal NPs have not been demonstrated. Herein, we reported structure-property of a class of highly polycrystalline plasmonic AuNPs, further indicating that grain size indeed can plays a key role in luminescence, surface plasmon and Raman enhancement properties of AuNPs. Because of luminescence, plasmon and Raman enhancement properties were successfully integrated in one single AuNP, these highly polycrystalline AuNPs can serve as multimodal probes for a variety of optical microscopic imaging techniques.

Experimental Section

Materials and equipment

All chemicals were purchased from Sigma-Aldrich or Fisher Sci. and used without further purification unless specified. Organic soluble CdSe/ZnS QDs (Qdot 655 ITK) were purchased from Invitrogen Inc. Thiolated cyclic RGD peptide was synthesized by and purchased from GL Biochem (Shanghai) Ltd. (Cat. No. RK-5 105524). Commercially gold NPs of 5 and 20 nm were purchased from Ted Pella Inc. A table-top centrifuge (Sarvall

Legand Micro 21) was used for NP purification and isolation. Particle size in the aqueous solution was determined by a Brookhaven 90Plus Dynamic Light Scattering Particle Size Analyzer (DLS). Electron Micrographic (EM) images were measured using a 200kV Jeol 2100 transmission electron microscope. The valence states of gold NPs were characterized by using a Perkin-Elmer X-ray photoelectron spectrometer (XPS) PHI 5600 ESCA system. Binding energies (BE) of Au $4f_{2/7}$ electrons were used as a signature to characterize Au oxidation states with alkyl chain C 1s BE (284.6 eV) as an internal reference. Absorption spectra of gold NPs were take nusing a Varian 50 Bio UV-Vis spectrophotometer. The luminescence spectrum of pAuNPs was collected under 532 nm laser excitation with power intensity of 5 kw/cm^2 using an Olympus IX-71 microscope coupled with an Acton Spectra-Pro 300i monochromator and a spectroscopy CCD camera (PIXIS Roper Scientific, Inc.). Ensemble SERS spectra of gold NPs were taken on a Jobin Yvon Horiba (France) LabRAM HR Raman Spectroscopy with a 1200 //mm grating. Raman scanning images were obtained from WITec alpha300R confocal Raman microscope (785 nm excitation) and constructed on the WITec project 2.02 software. Fluorescence images were obtained from an IX-71 inverted microscope (Olympus) with a 1.3NA 100X oil-immersion objective under Hg-lamp excitation (Ex: 532–587 nm; Em: 605–682 nm; 30 W/cm^2; 0.5 s exposure time) and a Photon Max 512 CCD camera (Princeton Instrument).

Synthesis of polycrystalline gold nanoparticles (pAuNPs)

The pAuNPs were synthesized in solid-state glycine matrices. Glycine of 250 mg and 13 mg $KAuCl_4$ were co-dissolved into 2 ml deionized water. After water evaporated, the mixture was then thermally reduced at 453 K in the solid state. When the color of the mixture became dark reddish, the reaction was stopped and the product was dissolved in 1 mL deionized water. The final solution was first centrifuged at 2,000 and 4,000 g for 2 min. respectively to remove the large aggregates. pAuNPs of ~20 nm were obtained by collecting the pellet after centrifuging the supernatant at 6,500 g for 3 min. The sample was further purified by centrifugation at 6,500 g for several times to remove the free ions and extra glycine ligand.

Bioconjugation of gold NPs

Mercaptobenzoic acid (MBA) methanol solution of 10 mM was diluted to 1 mM with 10 mM sodium borate buffer. PEG_{5000}-SH, as a ligand to prevent aggregation of gold NPs in aqueous solution, was dissolved in 10 mM sodium borate buffer to prepare 1 mM solution. The conjugation of MBA ligand to gold NPs was conducted by incubating the NPs with MBA and PEG_{5000}-SH at a molar ratio of $1:5\times10^4:5\times10^4$ in 10 mM sodium borate buffer for 1 hour with gentle shake. The sample was then centrifuged at 6,500 g for 3 min to collect the pellets and re-dissolved in distilled water.

The conjugation of pAuNPs with MBA and thiolated cRGD peptide was completed by incubating pAuNPs with thiolated cRGD and MBA at a molar ratio of $1:5\times10^4:5\times10^4$ in 10 mM sodium borate solution for 2 hours. The sample was then centrifuged at 6,500 g for 3 min. to collect the pellets and re-dissolved in phosphate buffer saline (PBS).

Cell culture

U87MG cells were cultured in DMEM (low glucose) supplemented with 10% (vol/vol) fetal bovine serum (FBS) and 1% penicillin-streptomycin (PS) at 5% CO_2, 37 °C. For cell labeling, U87MG cells were first fixed in PBS buffer solution using a mixture of 3.7% formaldehyde (Fisher Scientific) for 10 min. After aspirating the fixative and blocking the cells with 1 ml PBS buffer containing 2 wt % BSA for 30 min., we incubated the fixed cells with 1 nM pAuNPs in 500 μl PBS buffer solution at room temperature for 30 min. The fixed

cells were then washed thoroughly with PBS buffer to remove the excess amount of NPs and used for imaging studies.

Results and discussions

Monodispersed 20±4.5 nm AuNPs were obtained after the reaction and purification (Fig. 1a and Fig. S1) and the highresolution transmission electron microscopy (HR-TEM) studies showed that these AuNPs exhibit highly polycrystalline structures with grain size down to 1 nm (Fig. 1b and Fig. S2) while commercially available ~20 nm AuNPs (mAuNPs) synthesized in liquid phase exhibit multi-twinned structure with grains of 8 nm Inset in Fig. 1b). Selected area electron diffraction (SAED) ring pattern was observed from a pAuNP, indicating its highly polycrystalline nature and in contrast to the SAED pattern of mAuNPs (Fig. S3). The grain size distributions in the NPs were further quantified by investigating $4f_{7/2}$ electron binding energy (BE) of Au atoms in the NPs with X-ray photoelectron spectroscopy (XPS) because the core-electron BE shift of a metal atom is inversely proportional to the grain size of metallic thin films.[39] Fig. 1c shows that Au $4f_{7/2}$ BE of commercially available ~20 nm mAuNPs exhibits a single Gaussian peak at 83.9 eV, which is blue shifted 0.2 eV compared to bulk gold metal (83.7 eV),[40] while two peaks at 84.0 eV and 85.1 eV were observed from ~20 nm pAuNPs. The additional peak at 85.1 eV was comparable to BE (85.1 eV) of Au_{55} clusters (1.2 nm)[41] but lower than Au BE of gold oxides (Au_2O_3 or Au_2O) where Au $4f_{7/2}$ BEs in gold oxides are generally in the range from 85.6 to 86.5 eV.[42] Two BE shifts of 0.3 and 1.4 eV correspond to two different, 5 nm and 1 nm, grain-size populations in ~20 nm pAuNPs respectively, consistent with the observed highly polycrystalline structures of pAuNPs from TEM studies, indicating that the small grain sizes have been achieved with solid-phase methods for the synthesis of the pAuNPs. In contrast with traditional solution-phase method, in which crystal nuclei either become large crystals through rapid agglomeration or re-dissolve in the solution during the NP growth,[24, 43–44] this solid-phase synthesis likely provided a solid template for NP nucleation and stabilized the crystal nuclei during the NPs formation and thus prefers to produce pAuNPs instead of mAuNPs. Currently we are exploring the detailed growth mechanism of the pAuNPs, which will be reported in near future.

pAuNPs not only exhibit strong surface plasmon absorption but also enhanced Raman scattering as well as bright and robust single-particle luminescence. Shown in Figure 2a is the absorption maximum of ~20 nm as synthesized pAuNPs, which is red shifted about 16 nm compared to that of mAuNPs (520 nm). Since AuNPs with size comparable to EFW do not exhibit surface plasmons but single electron excitations and luminescence,[24, 45] the observed surface plasmons from pAuNPs must result from collective oscillations of free electrons in ~5 nm grains in the particles. By replacing the glycine on the pAuNPs with sodium citrate, the absorption maximum of pAuNPs is blue shifted back to ~526 nm (Fig. S4), indicating that the red shift observed from pAuNPs is likely caused by chemical effect.[46] In addition, after fitting the absorption spectra of AuNPs with Lorentzian function, we found that the surface plasmon bandwidth, a characteristic of collision efficiency between free electrons and surface atoms, of pAuNPs (105 nm) is much broader than that (81 nm) of the same size mAuNPs but comparable to that (107 nm) of 5 nm AuNPs, indicating that the dephasing of coherent oscillations of free electrons (surface plasmons) in pAuNPs was greatly enhanced by the increase of grain boundaries.[47–48]

Different from conventional plasmonic noble metal NPs that are often not luminescent due to extremely high density of states. Shown in Fig. S5 is the fluorescence image of ~ 20 nm mAuNPs where no fluorescence was observed. However, under the same excitation condition, pAuNPs exhibit strong luminescence at the single particle level (Fig. 3b). In addition, co-localization of the fluorescence image and dark-field image of pAuNPs

indicated that ~93% of the plasmonic pAuNPs were also luminescent species (Fig. S6), further confirmed that the observed fluorescence is indeed from the pAuNPs. The average emission intensity of individual pAuNPs is comparable to that of individual commercially available semiconductor quantum dots under the same mercury lamp excitation conditions (Fig. S7), suggesting that the emission cross section of pAuNPs is about 10^{-15} cm_2. Since surface plasmon absorption cross section of ~20 nm gold NPs is on the order of 10^{-13} cm^2,[49–50] the estimated quantum yield of pAuNPs is about 10^{-2} under such excitation conditions (See supplementary information for detail calculation). While luminescence quantum yield of pAuNPs is much smaller than those of few-atom nonplasmonic gold nanoclusters (10%~40%) because of strong surface plasmon absorption,[45] luminescence brightness and stability of pAuNPs at the single particle level are one order and three orders higher than those of few-atom nonplasmonic luminescent AuNPs respectively (Fig. S8).[51–53] Our lifetime measurements indicated that the luminescence lifetimes of pAuNPs is less than instrumental response function (~35 ps) of ultrafast laser system, which is more than two-order shorter than those of few-nm luminescent AuNPs.[51–53] The increase in luminescence intensity and stability and the decrease of lifetime are consistent with previous observations that fluorescence intensities of quantum dots and other fluorophores near a rough gold surface can be increased about one order by surface plasmons,[54–58] implying strong coupling between surface plasmons of large grains and single-electron excitations of small grains within a single particle. The advantage of these plasmonic nd luminescent pAuNPs over other known plasmon enhanced luminescence systems is that there is no need of conjugation of additional fluorophores and the dimension of pAuNPs is also much smaller than those known plasmonic luminescent nanostructures.[54–59]

Different from emission spectra of quantum dots, organic dyes and few-atom gold NPs, emission from pAuNPs is composed of not only luminescence from the small grains but also Raman emission peaks at 578 and 599 nm from glycine on pAuNPs Inset in Fig. 2b). The detailed Raman vibrations of glycine on the surface of pAuNPs were resolved with a 1200 // mm grating Fig. S9). While pAuNPs were synthesized in the glycine matrices and naturally coated by glycine molecules, Raman spectra of pAuNPs can be readily tuned by replacing glycine with other ligands. For example, by incubating glycine-pAuNPs with p-mercaptobenzoic acid (MBA) solution, we clearly observed characteristic Raman vibrations of MBA ligand[60–61] at 1071, 1132, 1173, 1579 cm^{-1}. The IR spectra indicate the MBA coverage on pAuNPs is ~1.75 times higher than that on mAuNPs Fig. S10), therefore, the overall Surface Enhanced Raman Scattering (SERS) intensity from MBA-pAuNPs is calculated to be ~7 times stronger than that from MBA-mAuNPs at the ensemble level (Fig. 2c). Using a characteristic vibration at 1579 cm^{-1}, we were able to image pAuNPs at the single particle level with a conventional scanning Raman microscope while most of mAuNPs were hardly observed under the same conditions (Fig. 2d and Fig. S11). Our observation that ~7 times magnitude increase in Raman enhancements observed from pAuNPs is consistent with the recent report with tip-enhanced Raman spectroscopy (TERS) that 1~2 nm roughness can increase Raman enhancement factors of Au tips nearly one order,[62] so we tentatively attribute this additional enhancement to the sharp surface features caused by the increase of grain boundaries, which further concentrate local electrical fields.[63–65]

Broad material properties of these highly polycrystalline AuNPs offer exciting opportunieis to address the challenges in the bioimaging. For example, while our fundamental understandings of cell biology have been greatly nurtured by the development of a variety of optical microscopic imaging techniques ranging from the simple bright-field microscope to the sophisticated sub-diffraction optical microscopic systems,[66–68] each optical imaging modality has its own limitations. For examples, bright-field optical microscopy generally is not suitable for imaging of membrane receptors because of its low sensitivity and disparity

of the receptors on the cell membrane, while fluorescence microscopic imaging techniques also have their own limitations including photobleaching, blinking and overlapping spectra of fluorophores. Due to these limitations in optical microscopic imaging techniques, to gain a comprehensive understanding of biomolecules of interest, significant efforts have been dedicated to developing multimodal probes that can integrate the strengths of different optical imaging techniques in the last few years.[69–70] With all the integrated optical properties, multifunctional pAuNPs provide an exciting opportunity for multimodality imaging. As a demonstration of applications of pAuNPs, here we applied them as a multi-modal nanoprobe for imaging of $\alpha_v\beta_3$ integrin receptors, a cancer receptor that is often over-expressed on U87MG cancer cells. To enable pAuNPs to selectively target $\alpha_v\beta_3$ integrin receptors and also detectable with Raman microscopy, we conjugated pAuNPs with MBA and a thiolated cRGD peptide, which exhibits high binding affinity (IC50=~8 nM) to $\alpha_v\beta_3$ integrin receptors on U87MG cancer cells.

Under mercury-lamp excitation, the diffraction limited fluorescence spots of MBA-pAuNPs-cRGD were readily observed on the U87MG cell membrane (Fig. 3a) and the blinking/intensity fluctuation was also observed, indicating that the majority of the NPs are mono-dispersed on the cell membrane while they were bound to the receptors. As control, we found that without cRGD peptide on the nanoparticle surface, very few MBA-pAuNPs were found on the cell membrane of U87MG cancer cells (Fig. S12a&b). After saturating $\alpha_v\beta_3$ integrin receptors with 1 mM free cRGD first, the MBA-pAuNPs-cRGD no longer bound to U87MG cancer cells (Fig. S12c&d). These studies confirmed that the conjugation of cRGD peptide to the NPs is responsible for the observed specific targeting of U87MG cells. Since the luminescence stability of pAuNPs at the single particle level is ~6 times and ~500 times higher than those of QDs and FITC respectively (Fig. S13), these luminescent pAuNPs are expected to further help unravel cellular dynamics at a high spatial and temporal resolution in the future.

The strong Raman enhancement of pAuNPs at the single particle level enables us to more readily image cancer cells with specific Raman signal. The Raman image of labeled U87MG cell can be constructed by utilizing the characteristic vibrations of MBA at 1579±10 cm^{-1} (Fig. 3b) using a confocal scanning Raman microscope. With strong SERS signal containing characteristic vibrations of both cRGD peptide and MBA, these MBA-pAuNPs-cRGD on the cell membrane also allows us to chemically image targeting molecule cRGD peptide. Fig. S14 shows a typical Raman spectrum of MBA-pAuNPs-cRGD on the labeled U87MG cells, where vibrations of amide I, II, III and phenyl ring of cRGD together with the vibrational modes of MBA were clearly observed.[71]

The surface plasmon absorption of pAuNPs is more than 300 times and ~104 times larger than the QD655s and FITC at the same concentrations in the visible range, respectively (Fig. S15). In contrast to the bright-field images of U87MG cells labeled by cRGD-FITC and cRGD-QD655s, strong surface plasmon absorption of conjugated MBA-pAuNPs-cRGD made the labelled U87MG cells pinkish and can be observed even with naked eyes (Fig. 3c), which offers a simple way for the detection of c-RGD receptors. The large surface plasmon scattering from MBA-pAuNPs-cRGD also allows us to image these cancer cells with a dark-field imaging technique at the single particle level (Fig. 3d). The success of integrating four different imaging modalities using a one single nanoprobe indicates that grain size engineering is a simple but versatile method for developing multifunctional metal NPs with enhanced properties with no need of conjugation of any additional fluorophores.

Conclusions

By growing AuNPs in a solid-state matrix, we were able to create highly polycrystalline AuNPs with grain size down to EFW. Differences in the material properties between pAuNPs and mAuNPs indicate that grain size effect also is a fundamental structure-property relationship in metal NPs as it is in metallic thin films. Using grain size effect, size-dependent material properties were engineered and enhanced in one single NP, which also provide a platform for fundamentally understanding of the couplings between quantum and classical size effects within a finite nanodomain. In addition, these multifunctional pAuNPs can serve as a robust multimodal imaging probe for four different optical imaging techniques and provide a foundation for integration of strengths of different, sometimes incompatible, imaging modalities together in the future.

Supplementary Material

Refer to Web version on PubMed Central for supplementary material.

Acknowledgments

This work was supported in part by NIH (1R21EB011762) and the start-up fund from the University of Texas at Dallas.

Notes and references

1. Kobrinsky MJ, Thompson CV. Acta Mater. 2000; 48:625.
2. Chae BG, Yang YS, Lee SH, Jang MS, Lee SJ, Kim SH, Baek WS, Kwon SC. Thin Solid Films. 2002; 410:107.
3. Zhang W, Brongersma SH, Clarysse T, Terzieva V, Rosseel E, Vandervorst W, Maex K. J. Vac. Sci. Technol. B. 2004; 22:1830.
4. Camacho JM, Oliva AI. Thin Solid Films. 2006; 515:1881.
5. Chuu DS, Dai CM. Phys. Rev. B. 1992; 45:11805.
6. Pande CS, Masumura RA. Mat. Sci.Eng. B-Solid. 1995; 32:247.
7. Zhao X, Schoenfeld O, Nomura S, Komuro S, Aoyagi Y, Sugano T. Mat. Sci.Eng. B-Solid. 1995; 35:467.
8. Braun F, von Delft J. Phys. Rev. B. 1999; 59:9527.
9. Jin S, Hwang SK, Morris JW. Metall. Trans.A. 1975; 6:1721.
10. Lasalmonie A, Strudel JL. J. Mat. Sci. 1986; 21:1837.
11. Feaugas X, Haddou H. Philos.Mag. 2007; 87:989.
12. Durkan C, Welland ME. Phys. Rev. B. 2000; 61:14215.
13. Karim S, Ensinger W, Cornelius TW, Neumann R. Physica. E. 2008; 40:3173.
14. Moskovits M. J. Chem. Phys. 1978; 69:4159.
15. Boyd GT, Yu ZH, Shen YR. Phys. Rev. B. 1986; 33:7923.
16. Tsybulya SV, Kryukova GN, Goncharova SN, Shmakov AN, Balzhinimaev BS. J. Catal. 1995; 154:194.
17. Parmenter RH. Phys. Rev. 1968; 166:392.
18. Natelson D, Willett RL, West KW, Peiffer LN. Solid. State. Comm. 2000; 115:269.
19. Zhu LL, Jin K, Zheng XJ. Appl. Phys. Lett. 2007; 91:103108.
20. Koshka Y, Ostapenko S, Tarasov I, McHugo S, Kalejs JP. Appl. Phys. Lett. 1999; 74:1555.
21. Bose S, Galande C, Chockalingam SP, Banerjee R, Raychaudhuri P, Ayyub P. J. Phys.-Condens. Mat. 2009; 21
22. Palasantzas G. Phys. Rev. B. 1998; 58:9685.

23. Bose S, Raychaudhuri P, Banerjee R, Vasa P, Ayyub P. Phys. Rev. Lett. 2005; 95:147003. [PubMed: 16241688]
24. Kreibig, U.; Vollmer, M. Optical Properties of Metal Clusters. Vol. Vol. 25. Springer; 1995.
25. Ashcroft, NW.; Mermin, ND. Solid State Physics. New York: HOLT, Rinehart and Winston; 1976.
26. Schaaff TG, Knight G, Shafigullin MN, Borkman RF, Whetten RL. J. Phys. Chem. B. 1998; 102:10643.
27. Wu Z, MacDonald MA, Chen J, Zhang P, Jin R. J. Am. Chem. Soc. 2011; 133:9670. [PubMed: 21634375]
28. Wu Z, Lanni E, Chen W, Bier ME, Ly D, Jin R. J. Am. Chem. Soc. 2009; 131:16672. [PubMed: 19886625]
29. Qian HF, Jin RC. Nano Lett. 2009; 9:4083. [PubMed: 19995083]
30. Sanchez A, Abbet S, Heiz U, Schneider WD, Häkkinen H, Barnett RN, Landman U. J. Phys. Chem. A. 1999; 103:9573.
31. Wallace WT, Whetten RL. J. Am. Chem. Soc. 2002; 124:7499. [PubMed: 12071759]
32. Campbell CT, Parker SC, Starr DE. Science. 2002; 298:811. [PubMed: 12399586]
33. Fedrigo S, Harbich W, Buttet J. J. Chem. Phys. 1993; 99:5712.
34. Chen W, Wang ZG, Lin ZJ, Lin LY, Fang KM, Xu Y, Su MZ, Lin JH. J. Appl. Phys. 1998; 83:3811.
35. Link S, Beeby A, FitzGerald S, El-Sayed MA, Schaaff TG, Whetten RL. J. Phys. Chem. B. 2002; 106:3410.
36. Peyser LA, Lee TH, Dickson RM. J. Phys. Chem. B. 2002; 106:7725.
37. Tang Y, Ouyang M. Nature Mater. 2007; 6:754. [PubMed: 17704781]
38. Zheng J, Ding Y, Tian BZ, Wang ZL, Zhuang XW. J. Am. Chem. Soc. 2008; 130:10472. [PubMed: 18636722]
39. Wertheim GK, Dicenzo SB. Phys. Rev. B. 1988; 37:844.
40. Fuggle JC, Kallne E, Watson LM, Fabian DJ. Phys. Rev. B. 1977; 16:750.
41. Turner M, Golovko VB, Vaughan OPH, Abdulkin P, Berenguer-Murcia A, Tikhov MS, Johnson BFG, Lambert RM. Nature. 2008; 454:981. [PubMed: 18719586]
42. Casaletto MP, Longo A, Martorana A, Prestianni A, Venezia AM. Surf. Interface Anal. 2006; 38:215.
43. Polte J, Ahner TT, Delissen F, Sokolov S, Emmerling F, Thünemann AF, Kraehnert R. J. Am. Chem. Soc. 2010; 132:1296. [PubMed: 20102229]
44. Abecassis B, Testard F, Spalla O, Barboux P. Nano Lett. 2007; 7:1723. [PubMed: 17530813]
45. Zheng J, Nicovich PR, Dickson RM. Annu. Rev. Phys. Chem. 2007; 58:409. [PubMed: 17105412]
46. Liedberg B, Lundstrom I, Wu CR, Salaneck WR. J. Colloid Interface Sci. 1985; 108:123.
47. Hostetler JL, Smith AN, Czajkowsky DM, Norris PM. Appl. Opt. 1999; 38:3614. [PubMed: 18319965]
48. Canchal-Arias D, Dawson P. Surf. Sci. 2005; 577:95.
49. Jain PK, Lee KS, El-Sayed IH, El-Sayed MA. J. Phys. Chem. B. 2006; 110:7238. [PubMed: 16599493]
50. Liu XO, Atwater M, Wang JH, Huo Q. Colloids Surf. B. 2007; 58:3.
51. Zhou C, Sun C, Yu M, Qin Y, Wang J, Kim M, Zheng J. J. Phys. Chem. C. 2010; 114:7727.
52. Zhou C, Long M, Qin YP, Sun XK, Zheng J. Angew. Chem. Int. Ed. 2011; 50:3168.
53. Yu M, Zhou C, Liu J, Hankins JD, Zheng J. J. Am. Chem. Soc. 2011; 133:11014. [PubMed: 21714577]
54. Shimizu KT, Woo WK, Fisher BR, Eisler HJ, Bawendi MG. Phys. Rev. Lett. 2002; 89:117401. [PubMed: 12225166]
55. Anger P, Bharadwaj P, Novotny L. Phys. Rev. Lett. 2006; 96:113002. [PubMed: 16605818]
56. Pompa PP, Martiradonna L, Della Torre A, Della Sala F, Manna L, De Vittorio M, Calabi F, Cingolani R, Rinaldi R. Nature Nanotechnol. 2006; 1:126. [PubMed: 18654164]
57. Chen Y, Munechika K, Ginger DS. Nano Lett. 2007; 7:690. [PubMed: 17315937]

58. Zhang JT, Tang Y, Lee K, Ouyang M. Nature. 2010; 466:91. [PubMed: 20596017]
59. Jin YD, Gao XH. Nature Nanotechnol. 2009; 4:571. [PubMed: 19734929]
60. Michota A, Bukowska J. J. Raman Spectrosc. 2003; 34:21.
61. Orendorff CJ, Gole A, Sau TK, Murphy CJ. Anal. Chem. 2005; 77:3261. [PubMed: 15889917]
62. Zhang WH, Cui XD, Yeo BS, Schmid T, Hafner C, Zenobi R. Nano Lett. 2007; 7:1401. [PubMed: 17447824]
63. Haynes CL, McFarland AD, Van Duyne RP. Anal. Chem. 2005; 77:338A.
64. Alvarez-Puebla R, Liz-Marzan LM, de Abajo FJG. J. Phys. Chem. Lett. 2010; 1:2428.
65. Pazos-Perez N, Barbosa S, Rodriguez-Lorenzo L, Aldeanueva-Potel P, Perez-Juste J, Pastoriza-Santos I, Alvarez-Puebla RA, Liz-Marzan LM. J. Phys. Chem. Lett. 2010; 1:24.
66. Murphy, DB. Fundamentals of Light Microscopy and Electronic Imaging. First ed.. Wiley-Liss; 2001.
67. Yildiz A, Selvin PR. Acc. Chem. Res. 2005; 38:574. [PubMed: 16028892]
68. Huang B, Bates M, Zhuang XW. Annu. Rev. Biochem. 2009; 78:993. [PubMed: 19489737]
69. Cheon J, Lee JH. Acc. Chem. Res. 2008; 41:1630. [PubMed: 18698851]
70. Kim J, Piao Y, Hyeon T. Chem. Soc. Rev. 2009; 38:372. [PubMed: 19169455]
71. Podstawka E, Sikorska E, Proniewicz LM, Lammek B. Biopolymers. 2006; 83:193. [PubMed: 16741975]

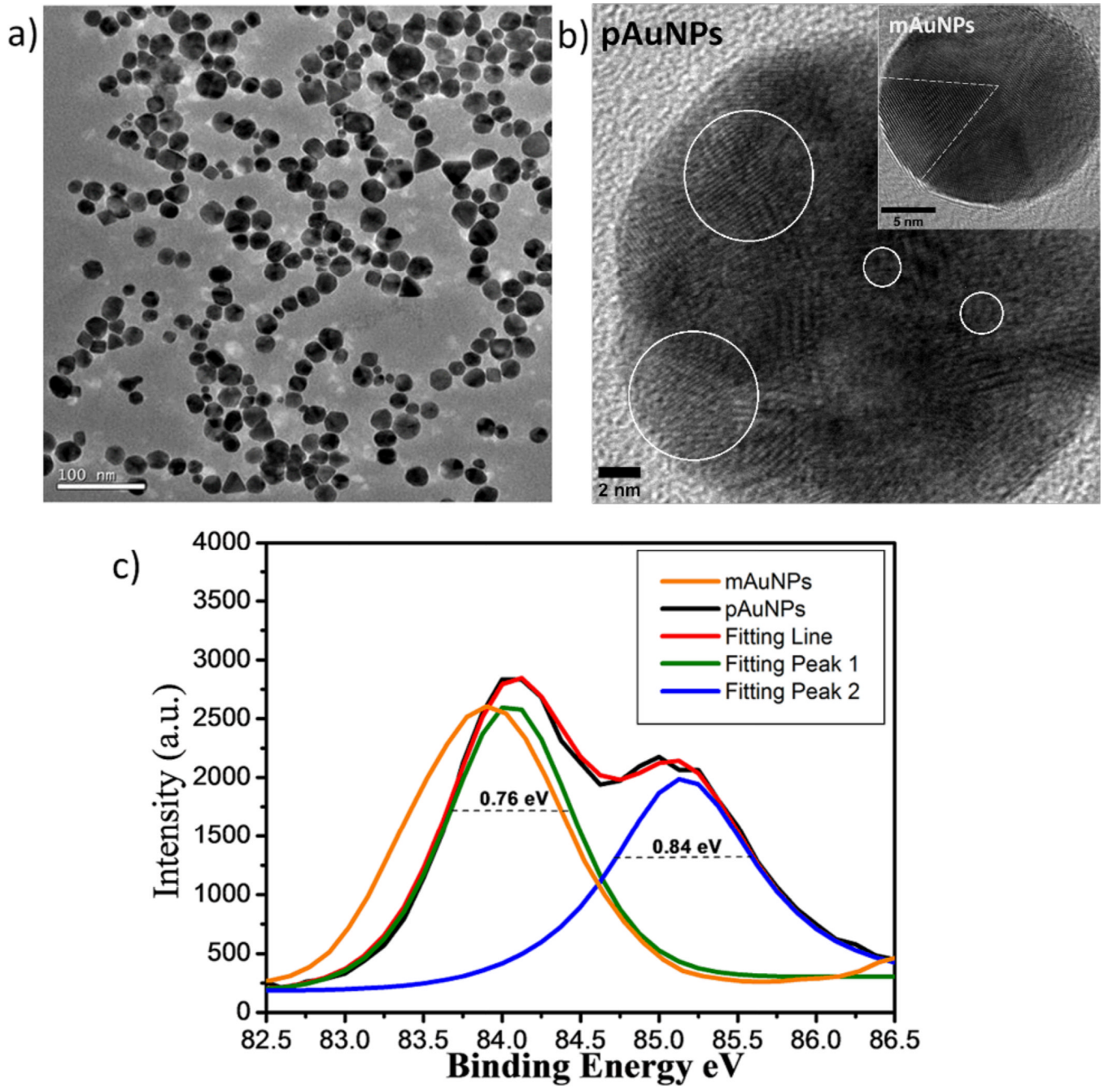

Figure 1.

pAuNPs created in glycine matrices through a solid-phase thermal reduction method. (a) pAuNPs of 20 nm were created after the reaction was completed. Inset: size distribution of pAuNPs by counting 150 particles. (b) HR-TEM image of pAuNPs, containing many grains with size down to 1 nm (scale bar: 2 nm), two ~5 nm and two ~1 nm representative individual grains are labelled with white circles; Inset: commercially available multi-twinned gold NP (mAuNP) composed of 8 nm grains (scale bar: 5 nm). (c) X-ray photoelectron spectroscopic measurements on Au 4f7/2 binding energy (BE) of pAuNPs and mAuNPs. Two peaks with maxima at 84.0 eV and 85.1 eV were observed from ~20 nm pAuNPs while only one peak at 83.9 eV was observed from the same size mAuNPs.

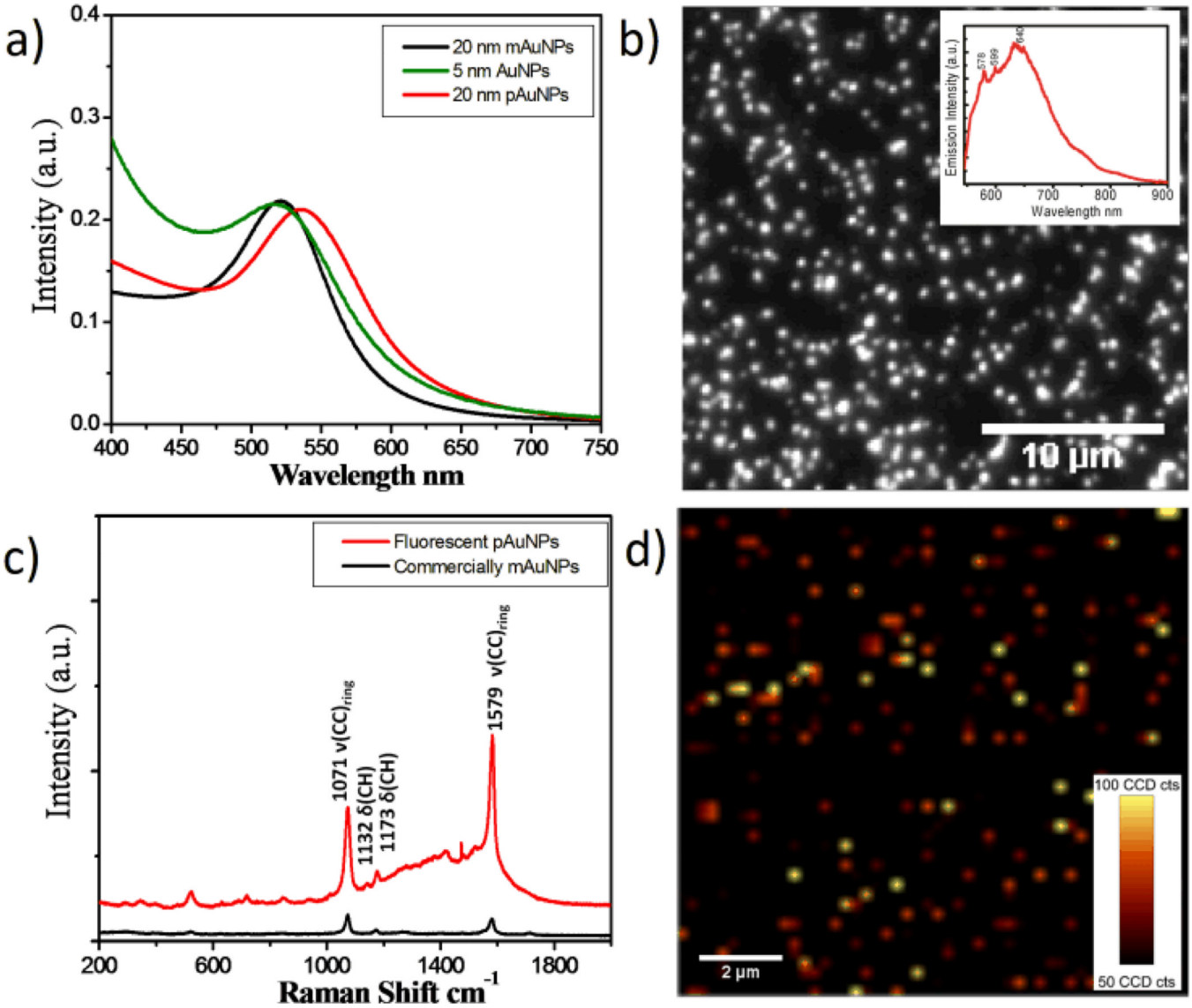

Figure 2.

Optical properties of pAuNPs. (a) UV-Vis absorption spectra of as synthesized 20 nm pAuNPs, 20 and 5 nm mAuNPs aqueous solutions. The surface plasmon maximum of pAuNPs is located at 536 nm, which is red shifted about 16 nm compared to those of 5 and 20 nm mAuNPs. (b) Fluorescence image of individual pAuNPs. Inset: emission spectrum of pAuNPs under 532 nm laser excitation. (c) Raman spectra of pAuNPs and mAuNPs coated by p-mercaptobenzoic acid (MBA) molecules. (d) Raman image of individual MBA-pAuNPs were constructed based on the vibration at 1579±10 cm^{-1}.

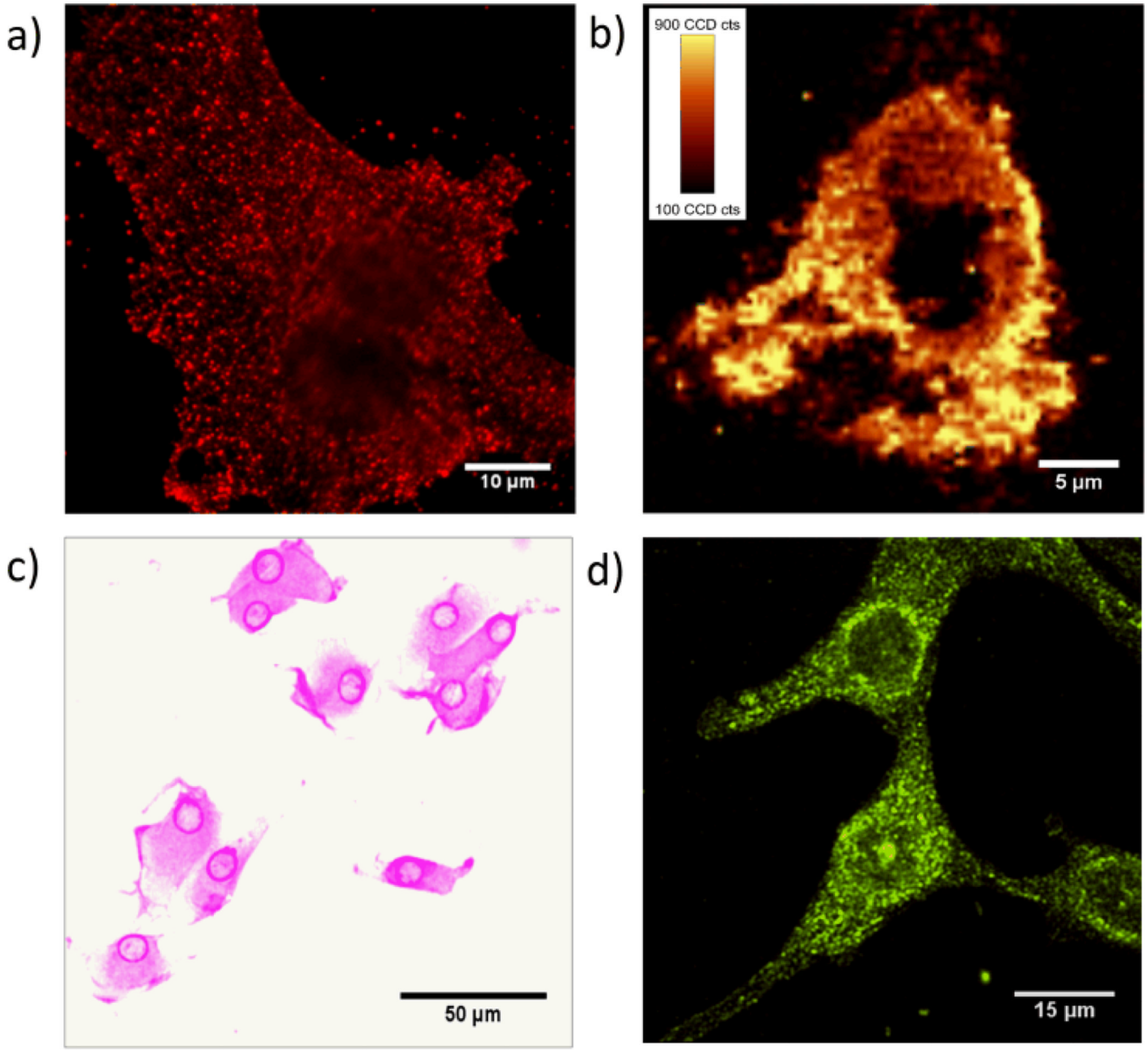

Figure 3.

MBA-pAuNPs-cRGD served as a multi-modality probe that enables $\alpha_v\beta_3$ integrin receptors on U87MG cancer cells to be imaged with four different imaging techniques at the single cell level. (a) Strong single-particle luminescence from pAuNPs enabled the integrin receptors on a single U87MG cell to be imaged using fluorescence microscopic imaging modality. (b) Raman image of a U87MG cancer cell labeled by cRGD-pAuNPs-MBA, which was constructed based on the Raman vibration of MBA at 1579±10 cm-1(fluorescence background was substracted). (c) Bright-field image of the cancer cells labeled by the NPs. Strong surface plasmons of the pAuNPs made the cells purplish. (d) Strong surface plasmon scattering of pAuNPs allow the cancer cells to be visualized using dark-field imaging modality.